# RESEARCH ARTICLE



**Droplet** WILEY

# Thermo-magnetic soft robot for adaptive locomotion and delivery

Yutong Wang<sup>1</sup> | Shenghao Yang<sup>1</sup> | Chonglei Hao<sup>1</sup> | Binhong Dou<sup>1</sup> | Lei Zhang<sup>1</sup> | Yongle Feng<sup>1</sup> | Shichuan Wang<sup>1</sup> | Fuzhou Niu<sup>2</sup> | Ran Tao<sup>1,3</sup> | Sen Wang<sup>1</sup> Bing Li<sup>1</sup> | Zuankai Wang<sup>4</sup> •

# Correspondence

Chonglei Hao and Bing Li, School of Mechanical Engineering and Automation. Harbin Institute of Technology, Shenzhen 518055, China.

Email: haoc@hit.edu.cn and libing.sgs@hit.edu.cn

Zuankai Wang, Department of Mechanical Engineering, The Hong Kong Polytechnic University, Hong Kong 999077, China. Email: zk.wang@polyu.edu.hk

# **Funding information**

Shenzhen Science and Technology Program, Grant/Award Numbers: JCYJ20210324132810026. KOTD20210811090146075 GXWD20220811164014001: National Natural Science Foundation of China, Grant/Award Numbers: 52375175, 52005128; Guangdong Basic and Applied Basic Research Foundation, Grant/Award Number: 2024A1515240015

### **Abstract**

Soft robots based on stimuli-responsive materials, such as those responsive to thermal, magnetic, or light stimuli, hold great potential for adaptive locomotion and multifunctionality in complex environments. Among these, liquid crystal elastomers (LCEs) and magnetic microparticles have emerged as particularly promising candidates, leveraging their thermal responsiveness and magnetic controllability, respectively. However, integrating these modes to achieve synergistic multimodal actuation remains a significant challenge. Here, we present the thermo-magnetic petal morphing robot, which combines LCEs with embedded magnetic microparticles to enable reversible shape morphing via remote light-to-thermal actuation and high-speed rolling locomotion under external magnetic fields. The robot can achieve rapid deformation under nearinfrared light, transitioning from a closed spherical to an open cross-like configuration with consistent shape recovery across multiple cycles, and demonstrates a maximum locomotion speed of 30 body lengths per second, outperforming many state-of-theart soft robots. Moreover, the robot's performance remains robust across dry, wet, and underwater conditions, with adjustable magnetic particle concentrations allowing tunable actuation performance. Our work addresses the need for soft robots with enhanced versatility and adaptability in complex environments, paving the way for applications in areas such as targeted drug delivery and industrial material handling.

Yutong Wang, Shenghao Yang and Chonglei Hao contributed equally to this study.

This is an open access article under the terms of the Creative Commons Attribution License, which permits use, distribution and reproduction in any medium, provided the original work is properly cited.

© 2025 The Author(s). Droplet published by Jilin University and John Wiley & Sons Australia, Ltd.

<sup>&</sup>lt;sup>1</sup>School of Mechanical Engineering and Automation, Harbin Institute of Technology, Shenzhen, China

<sup>&</sup>lt;sup>2</sup>School of Mechanical Engineering, Suzhou University of Science and Technology, Suzhou, China

<sup>&</sup>lt;sup>3</sup>School of Physics, University of Electronic Science and Technology of China, Chengdu, China

<sup>&</sup>lt;sup>4</sup>Department of Mechanical Engineering, The Hong Kong Polytechnic University, Hong Kong, China

#### INTRODUCTION

The field of soft robotics has seen significant progress in recent years, driven by the development of materials that respond to external stimuli such as light, heat, or magnetic fields, enabling adaptive motion, shape morphing, and environmental sensing. 1-5 These advancements have opened up new possibilities for robotic systems capable of operating in complex and unpredictable environments, from biomedical applications to industrial automation.<sup>6</sup> Among the various stimuli-responsive materials, liquid crystal elastomers (LCEs) have emerged as particularly promising candidates for soft robotic applications due to their ability to generate large, programmable, and fully reversible actuation strains in response to thermal stimuli.<sup>7-9</sup> Specifically, LCEs undergo a nematic-to-isotropic phase transition above their critical temperature, during which the LCs transition from an ordered to a disordered state, causing macroscopic contraction along the direction of mesogen alignment. 10 When cooled, the LCEs recover their initial alignment and shape, enabling fully reversible deformation. This thermo-mechanical behavior not only provides significant shape changes but also supports high energy density deformation, making LCEs ideal candidates for soft robotic actuation. 11-13 However, traditional thermal actuation techniques, including joule heating, hot plates, and hot water baths, present challenges in achieving precise, localized, and untethered heating, particularly in confined environments. 14,15 For instance, Joule heating requires tethered connections that restrict mobility, while other methods often result in uniform heating, limiting their effectiveness for selective actuation. 16-19

To address these challenges, magnetic actuation has emerged as a promising alternative or complementary strategy. Magnetic fields, especially in combination with embedded ferromagnetic particles. allow for non-contact control and provide a versatile mechanism for driving soft robots in diverse environments. 20,21 Soft magnetic robots incorporating NdFeB magnetic microparticles (NMMPs) have demonstrated functionalities such as rolling, swimming, and targeted object manipulation, facilitating robust operation across a variety of conditions. Despite these advancements, the combined use of thermal and magnetic actuation remains relatively underexplored within the context of soft robotics, particularly for achieving complex morphing behaviors and versatile locomotion.<sup>22-25</sup> For magnetic soft robots, while they offer excellent control and navigation capabilities, they often struggle with generating large deformations or complex shape changes. Additionally, the incorporation of magnetic particles can significantly alter the mechanical properties of the soft matrix, potentially limiting the robot's flexibility and adaptability.<sup>26</sup> Recent efforts to address these challenges have explored various strategies, including the development of composite materials that combine LCEs with other functional components.<sup>27-29</sup> These approaches aim to create multiresponsive systems that can be actuated through different stimuli, potentially overcoming the limitations of single-mode actuation. However, achieving a synergistic combination of thermal and magnetic actuation in a cohesive and efficient system continues to be an area of active research.

In this study, we introduce the thermo-magnetic petal morphing robot (TMPMR), a soft robotic platform that synergistically combines the thermal responsiveness of LCEs with the magnetic actuation capabilities of embedded NdFeB microparticles. This integration enables the TMPMR to perform two core functions: reversible shape morphing via thermal actuation and controlled rolling locomotion under magnetic fields. Leveraging these dual actuation mechanisms, the TMPMR achieves rapid, untethered, and selective actuation, addressing the longstanding challenges faced by existing LCE-based soft robots. Experimental results demonstrate that the TMPMR achieves consistent deformation and recovery under near-infrared (NIR) light while exhibiting robust locomotion across diverse environments, including dry, wet, and underwater conditions. These advancements open up exciting possibilities for applications such as targeted drug delivery, environmental monitoring, and industrial material handling. By addressing key limitations in soft robotic actuation, the TMPMR can contribute to the broader understanding and development of multi-

responsive soft robotic systems, paving the way for versatile and

adaptive robots capable of functioning in challenging environments.

### **RESULTS AND DISCUSSION**

The TMPMR is designed to integrate both thermal and magnetic actuation mechanisms, providing it with dual functionalities: cargo manipulation and rolling locomotion. As shown in Figure 1a, the TMPMR consists of a spherical body with four petal-like appendages that morph between open and closed states. This design allows the robot to encapsulate and transport cargo efficiently. The LCE material, specifically RM257, is responsible for the robot's thermal responsiveness, while embedded NMMPs, with detailed parameters shown in Supporting Information: Table S1, enable magnetic control. The inclusion of dopamine hydrochloride (DAH) coatings imparts photothermal properties, allowing the robot to convert NIR light into heat, thus driving thermal actuation.

The synthesis of the TMPMR involves a two-step polymerization process, as depicted in Figure 1b. In the first stage, the LCE was crosslinked to form an elastic network. Following mechanical stretching, the LCE molecules aligned along the direction of the applied force, transitioning from an isotropic to a LC phase. This alignment is critical to the TMPMR's ability to undergo shape morphing upon heating. Subsequent ultraviolet (UV)-induced polymerization fixed the aligned structure, ensuring that the TMPMR can reliably transition between its open and closed states. The optical images in Figure 1c demonstrate this transition, where the LCE becomes transparent after mechanical stretching, indicating molecular alignment. As shown in Figure 1d, cross-sectional scanning electron microscope (SEM) images display the distribution of NdFeB microparticles within the TMPMR for different NdFeB-to-LCE mass ratios  $\varphi$  of 1:8, 1:4, and 1:2, respectively. Due to the higher density of NMMPs compared to LCEs, the particles are predominantly located at the bottom of the cross-sectional samples, rather than uniformly dispersed throughout the material. False

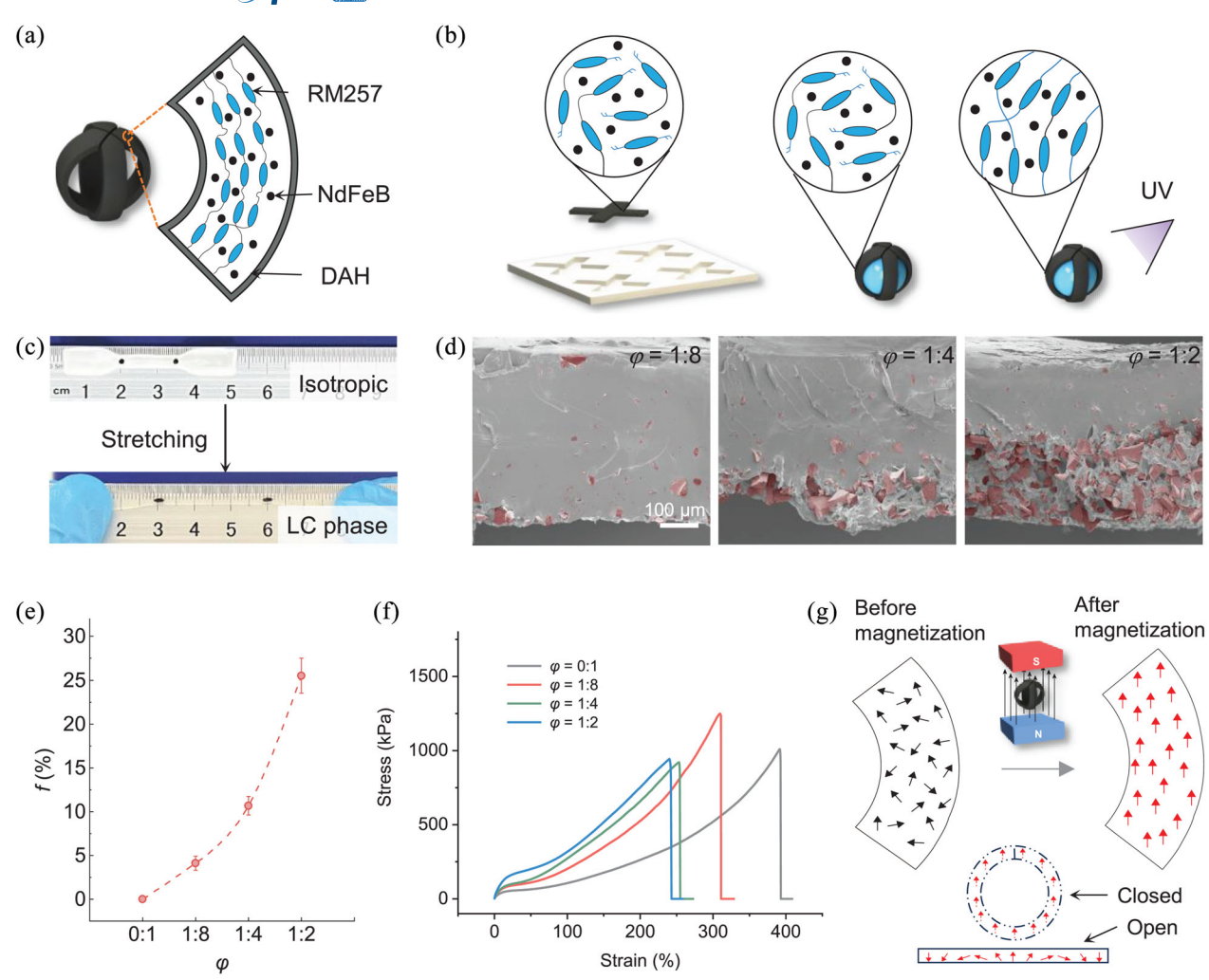


**FIGURE 1** Design, synthesis, and characterization of thermo-magnetic petal morphing robots (TMPMRs). (a) Schematic representation of the spherical TMPMR, featuring four petal-like appendages, and its constituent materials. (b) Illustration of the two-step synthesis process used to fabricate the TMPMR. (c) Optical images of the uniaxially aligned liquid crystal elastomer (LCE), showing the phase transition from isotropic to liquid crystal (LC) phase under mechanical stretching. (d) Cross-sectional scanning electron microscopy (SEM) images of the composite LCE material. False coloring highlights the distribution of NdFeB microparticles with different concentrations. (e) Surface coverage fraction of microparticles as a function of NdFeB-to-LCE mass ratio ( $\varphi$ ), calculated from image analysis in (d). (f) Stress-strain curves of composite LCEs with various concentrations of NdFeB microparticles, demonstrating differences in mechanical properties. (g) Schematic showing the magnetization profile of the TMPMR before and after the magnetization process, with NdFeB magnetic microparticles (NMMPs) incorporated. Lower panel illustrates the magnetization profile of the robot's petal-like appendages in their closed and open states.

coloring was applied to these SEM images to enhance visibility, with the NMMPs highlighted in red to emphasize their concentration at different ratios. The energy-dispersive spectroscopy analysis of iron element for various samples further validated their distribution near the bottom of TMPMRs (Supporting Information: Figure S1). Figure 1e provides further quantitative validation by analyzing the surface coverage rate of NMMPs for the different mass ratios. Indeed, the surface coverage increases proportionally with the NdFeB-to-LCE ratio, confirming that higher concentrations of NMMPs result in more particles precipitated along the surface. Figure 1f presents the stress–strain curves for TMPMR samples with varying NdFeB-to-LCE mass ratios. The data show that for our prepared samples, increasing the concentration of NMMPs does not consistently lead to higher stress values across the strain ranges. While intermediate concentrations

(e.g.,  $\varphi=1:8$ ) exhibit higher stress at lower strain levels compared to the pure LCE sample ( $\varphi=0:1$ ), the relationship between NdFeB concentration and mechanical performance is not linear. The pure LCE sample demonstrates the highest elongation at break ( $\sim380\%$ ), indicating that the addition of NMMPs reduces the composite's flexibility. However, higher NdFeB concentrations do not guarantee increased load-bearing capacity, as reflected in the measured stress. These results suggest that while the incorporation of NMMPs may enhance magnetic responsiveness and contribute to structural stiffness, there is a trade-off between flexibility and mechanical performance, and further optimization of the particle concentration is required based on specific applications. Figure 1g further illustrates the magnetization procedure and its effect on the embedded NMMPs. Prior to the magnetization process, the NMMPs exhibit a random magnetic orientation (Figure 1g,

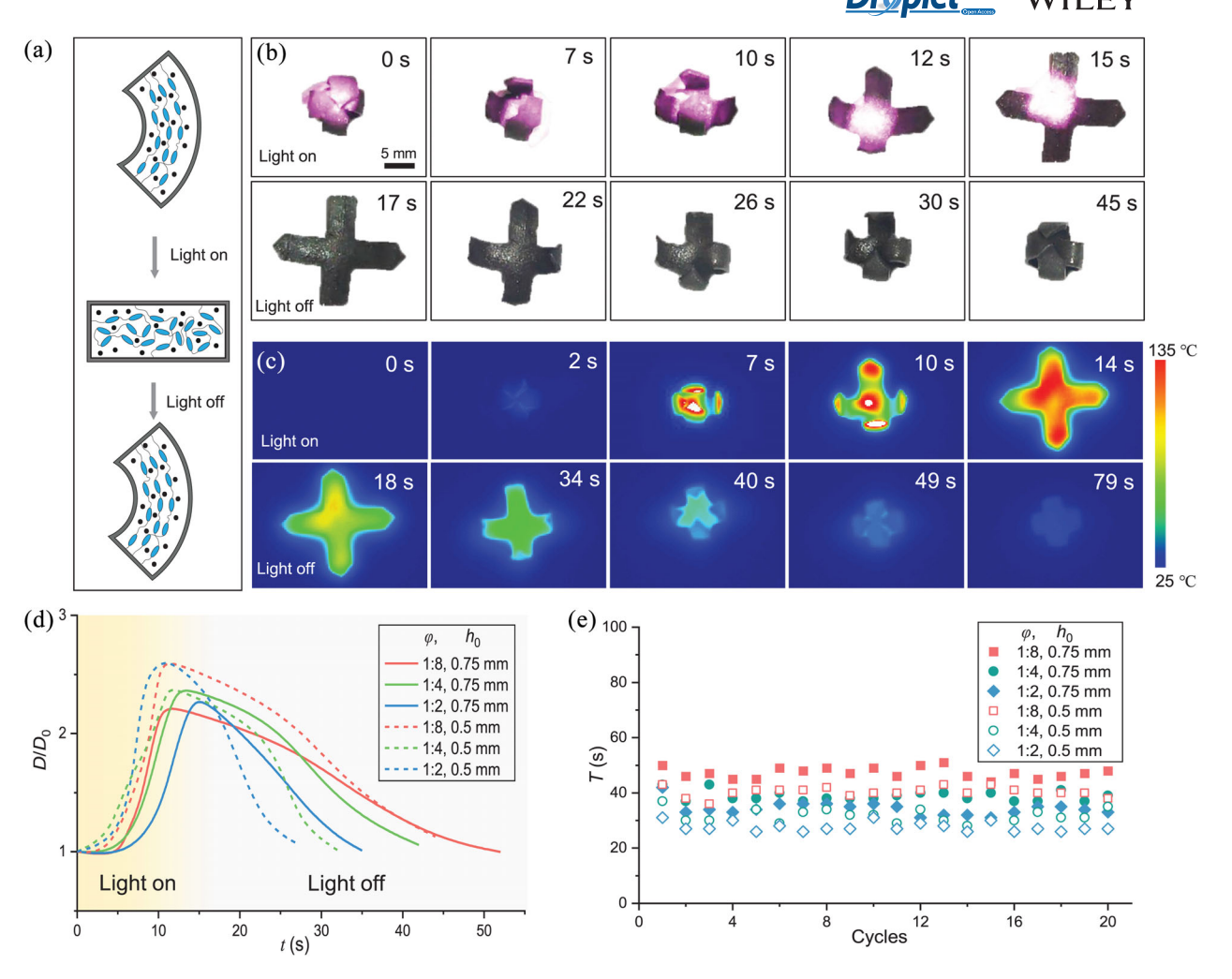


FIGURE 2 Thermal response of the thermo-magnetic petal morphing robot (TMPMR). (a) Schematic showing the deformation of the TMPMR's petals when actuated by near-infrared (NIR) light, demonstrating the reversible transition between liquid crystal (LC) and isotropic phases. (b) Optical images capturing the TMPMR's shape change under exposure to NIR light (~4700 mW/cm²) during on/off cycles. (c) Infrared thermographic images showing the surface temperature distribution during NIR light-induced actuation. (d) Normalized size variation of the TMPMR as a function of time during one light on/off cycle, with maximum deformation reaching a factor of approximately 2.6. (e) Response time measurements over multiple light on/off cycles, illustrating the long-term stability of TMPMR's thermal response.

upper-left panel). Upon exposure to a strong impulse magnetic field, the magnetic moments of the particles align with the field direction, resulting in a unidirectional magnetic configuration (Figure 1g, upper-right panel). This alignment is essential for generating the magnetic torque needed for the TMPMR's rolling locomotion. In addition, the lower panel of Figure 1g demonstrates the magnetic alignment profile of the robot's petal-like appendages during open and closed states. Considering the robustness requirements for TMPMR operation in various environments, a superhydrophobic treatment was applied to its surface. This treatment reduced adhesion of liquid and solid contaminants, minimized surface adhesion, and enhanced the robot's self-cleaning capability, achieving a water contact angle of approximately 158° (Supporting Information: Figure S2).

The TMPMR exhibits reversible shape morphing behavior under NIR light of 808 nm irradiation, driven by the thermal responsiveness of its LCE matrix. As schematically shown in Figure 2a, when the NIR light is turned on, the robot's petals transition from a closed spheri-

cal configuration to an open cross-like shape due to the LCE molecules contraction by the LC-to-isotropic phase change, which occurs at a critical temperature of approximately 62°C. Upon turning off the light, the petals return to their closed state. In our experimental setup, NIR light with intensity of about 4700 mW/cm<sup>2</sup> was used to actuate the TMPMR. and two distinct thicknesses of LCE/NMMPs composite films were used during fabrication, denoted as  $h_0 = 0.75$  and 0.5 mm, to evaluate the effect of thickness on thermal response. As shown in Figure 2b, the petals' shape transformation of TMPMR ( $\varphi = 1.8, h_0 = 0.75$  mm) occurs within seconds of light exposure, with petals reaching full opening state in about 15 s. Then the petals gradually curled toward the center after turning off the light, and returned to the original state at time of about 45 s. The accompanying thermographic images (Figure 2c) provide insight into the surface temperature distribution during this process, revealing a significant increase in temperature localized to the areas exposed to NIR light. It is noted that the robot has not yet cooled down to room temperature when it closed completely. This leads to

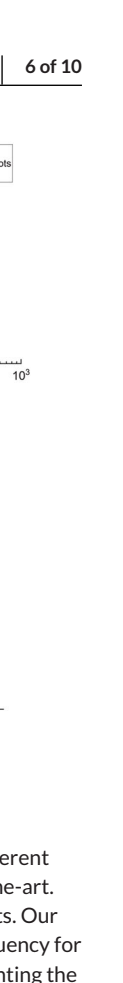
the situation where, after the robot closed but not vet fully cooled down, it has a faster response time to the second stimulus. The residual heat acted as a "pre-heating" mechanism, resulting in reduced opening times for subsequent cycles (Supporting Information: Figure S3). Since the closing process relied on passive air cooling, its duration remained largely consistent across all cycles. In addition, the characterized dimensionless size variation of the TMPMR  $D/D_0$  as a function of time during light exposure is presented in Figure 2d, where D represents the diameter of projected area of our spherical TMPMR on the horizontal plane, and  $D_0$  is the initial diameter before the light exposure. Overall, our various TMPMRs are capable of achieving a maximum deformation in range of 2.1-2.6, indicating substantial morphing capability. Obviously for this configuration, the opening process consistently occurs faster than the closing process. The influence of LCE/NMMPs composite thickness was also examined, with samples of  $h_0 = 0.75$  and 0.5 mm showing consistent deformation patterns, though the thinner sample ( $h_0 = 0.5$  mm) exhibited a slightly faster response time. Moreover, the samples with higher NdFeB mass ratio demonstrate faster recovery to the closed state. This is probably because the amount of NMMPs incorporated into the LCE matrix significantly impacts the stiffness of the TMPMR, as robots with higher NMMPs content exhibit greater rigidity. This rigidity, in turn, accelerates the robot's closing operation after the NIR light is switched off, allowing the petals to fold back into their spherical shape more quickly. Importantly, the characterized total response time remains consistent over multiple cycles of actuation for various tested samples, as shown in Figure 2e. This stability suggests that the TMPMR can be used for long-term operations without significant degradation in performance. Meanwhile, the response time of TMPMRs can also be affected by the variation of applied NIR light intensity. As we reduce the light intensity to about 220 mW/cm<sup>2</sup>, the opening time for TMPMR can be significantly increased compared to those with 4700 mW/cm<sup>2</sup> (Supporting Information: Figure S3). Unless otherwise noted, all subsequent experiments characterizing the motion performance were performed using TMPMR samples with a thickness of 0.5 mm.

The TMPMR's rolling locomotion is driven by an external rotating magnetic field, enabled by the internal alignment of NMMPs. The details of magnetic field control for robot manipulation can be found in Supporting Information: Notes S1-S3 and Figure S4. Figure 3a depicts the robot's characterized locomotion speed as a function of magnetic field strength B under a fixed magnetic field rotation frequency of 4 Hz. Specifically, below a threshold of approximately 1.1 mT (greenshaded region), the magnetic field strength is insufficient to generate enough torque to overcome friction, leaving the robot in an immobilized state. Once the magnetic field strength exceeds a higher threshold of about 1.5 mT (gray-shaded region), the TMPMR exhibits stable rolling motion, with its speed reaching a steady value of approximately 110 mm/s. In this regime, the robot's motion becomes smooth and reliable, showing no significant fluctuations in speed. However, within the range between 1.1 and 1.5 mT (yellow-shaded region), although the TMPMR begins to roll, its motion is highly unstable. This instability manifests as significant fluctuations in speed and noticeable lateral shaking of the robot on the horizontal plane. The primary reason for

this erratic behavior is that, within this voltage range, the magnetic field strength is insufficient to generate a consistent driving torque greater than the frictional forces acting on the robot. As a result, the TMPMR struggles to maintain stable motion, frequently starting and stopping. The robot's rolling is periodically interrupted as the driving torque decreases and can no longer sustain movement, leading to repeated cycles of acceleration and deceleration, or even momentary halts. This dynamic creates the observed instability in both the speed and trajectory of the robot.

The rolling locomotion of the TMPMR is driven by the interaction between the robot's magnetic moment M and the applied magnetic field **B**, which generates a torque that induces angular acceleration  $\alpha$ . As the robot's speed increases, the angle  $\delta$  between **M** and **B** decreases, reducing the angular acceleration until the robot reaches a stable rolling velocity. In essence, when the magnetic field is strong enough, the TMPMR's speed synchronizes with the rotating magnetic field, meaning that an increase in the field's rotation frequency results in a proportional increase in the robot's rolling speed. To investigate the relationship between the robot's rolling speed and the magnetic field's rotation frequency, the magnetic field control voltage was set to 10 V, and the rotation frequency was incrementally increased (1, 4, 7, and 10 Hz). Figure 3b shows time-lapsed images of the TMPMR's rolling trajectory ( $\varphi = 1:4$ ) on a dry surface at specific time intervals of 0, 150, 300, and 450 ms, respectively, corresponding to the rows from top to bottom in each column, while Figure 3c presents the corresponding displacement-time curves. As the frequency increases, the TMPMR's displacement increases, indicating that higher rotation frequencies result in faster rolling speeds. We also compare the speed and body length (BL) of various state-of-the-art robots, including LCE robots<sup>8,16,30-39</sup> and magnetically controlled robots,<sup>22,24,25,40-49</sup> with our TMPMR marked by the red star, as shown in Figure 3d. The plot shows speed normalized by BL/s, allowing for a direct comparison of locomotion efficiency across these categories. Our TMPMR is capable of achieving a maximum speed of approximately 30 BL/s, placing it at the higher end of the performance spectrum for both LCE and magnetic robots. Notably, magnetic robots (blue diamonds) tend to cluster around a lower speed range, with most achieving speeds below 10 BL/s. The TMPMR's combination of light-responsive LCEs and magnetic actuation enables it to reach speeds that are competitive with both LCE and magnetic robots. Additionally, the TMPMR's simple design allows for this high-speed rolling motion without the complexity of more bio-inspired robots, making it a more versatile option for certain applications. It also highlights that while robots using LCEs (orange circles) can exhibit a range of speeds, they typically fall below the performance levels achieved by our TMPMR. This suggests that the combination of thermal and magnetic actuation in our design results in significantly improved locomotion capabilities compared to LCE-based systems that rely solely on thermal actuation.

To further explore the effect of NMMPs concentration on rolling performance, we compared the average rolling speeds of TMPMRs with various mass ratios ( $\varphi = 1.8$ , 1.4, and 1.2). Figure 3e shows that when the magnetic field strength is sufficient to induce stable rolling, increasing the rotation frequency leads to a linear increase in speed,



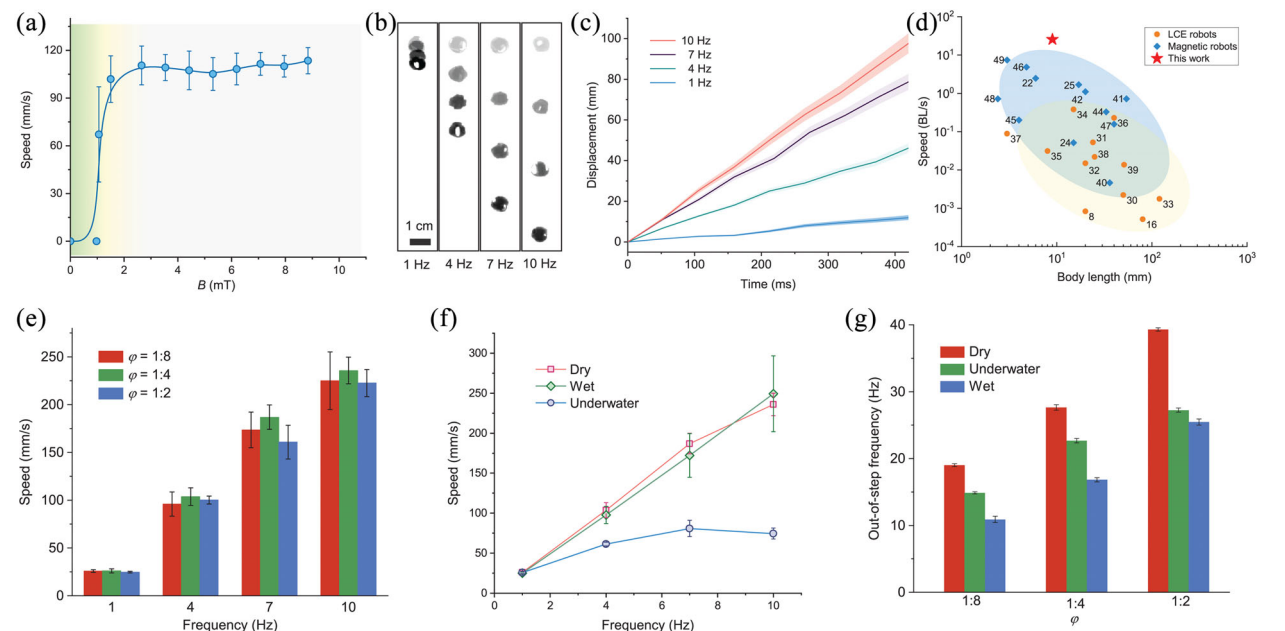


**FIGURE 3** Locomotion performance of the thermo-magnetic petal morphing robot (TMPMR) under various conditions. (a) TMPMR's locomotion speed as a function of magnetic field strength *B*, with a fixed magnetic field rotation frequency of 4 Hz. (b) Time-lapsed images demonstrating the TMPMR's movement under different magnetic field rotation frequencies. (c) Measured displacement over time for different rotation frequencies, showing how actuation efficiency varies. (d) Maximum locomotion speed of the TMPMR compared to the state-of-the-art. Comparison of maximal locomotion speed relative to body length (BL), with shaded regions representing different categories of soft robots. Our TMPMR, marked by the red star, achieves a maximum speed of approximately 30 BL/s. (e) Locomotion speed as a function of rotation frequency for TMPMRs with different NdFeB microparticle concentrations. (f) Speed variation in different environments (dry, wet, underwater), highlighting the TMPMR's versatility. (g) Characterization of the instability frequencies beyond which the TMPMR's motion cannot synchronize with the external magnetic field, analyzed for different environments and microparticle concentrations.

regardless of NMMPs' concentration. It indicates that while the concentration of NMMPs affects the generated magnetic torque, it does not significantly influence the robot's speed once stable motion is achieved under the same field conditions.

Given that the TMPMR may be deployed in various environments, we also examined and compared its rolling performance on dry, wet, and even underwater environments, respectively. Here we used a TMPMR with  $\varphi=1:4$  and set the magnetic field control voltage to 10 V. Figure 3f shows that the robot's speed in wet environments is comparable to that in dry conditions across a range of frequencies. However, in underwater environments, the increase in speed with rising frequency is less pronounced, with a maximum speed of approximately 73 mm/s. Further increases in rotation frequency do not yield significant speed gains. Additionally, the robot exhibited more stable and uniform motion underwater, with smaller speed variations compared to dry and wet environments.

Interestingly, at higher magnetic field rotation frequencies, a different behavior was observed. When the field rotates too fast, the angle  $\delta$  can exceeds 90°, causing the driving torque to decrease. This reduces the robot's angular acceleration, and as  $\delta$  continues to increase, the torque further diminishes. If  $\delta$  reaches 180°, the torque reverses direction, leading to erratic motion such as oscillation or vibration, where the TMPMR can no longer synchronize with the magnetic field. This behavior, analogous to "slip" in motors, sets an upper limit for the robot's stable rolling frequency, referred to as the

"out-of-step frequency." Figure 3g shows the characterized out-of-step frequencies for TMPMRs with different NMMPs' concentrations. The results briefly indicate that increasing the concentration of NMMPs raises the step-out frequency, allowing the robot to roll at higher field rotation speeds. On the other hand, the step-out frequency is lower in underwater environments compared to dry conditions, and it decreases further in wet conditions.

To better understand the impact of magnetic field strength on the locomotion performance, we further conducted experiments to demonstrates the influence of NMMPs concentration ( $\varphi = 1.8, 1.4, \text{ and}$ 1:2) on the critical magnetic field strength required for the actuation of TMPMRs across different environments, including dry (Figure 4a), wet (Figure 4b), and underwater (Figure 4c) conditions. Briefly, across all environments, increasing the mass ratio  $\varphi$  reduces the critical magnetic field strength required for actuation, as indicated by the yellow regions. This effect is particularly pronounced in wet environments (Figure 4b), where the critical magnetic field strength significantly decreases with higher NMMPs concentrations. For instance, for  $\varphi = 1.8$ , the critical magnetic field strength in the wet environment under the rotation frequency of 4 Hz is 5.17  $\pm$  0.31 mT, but this decreases to 0.97  $\pm$  0.35 mT when  $\varphi$  is increased to 1:2. In comparison, the reduction is less prominent on dry surfaces and underwater conditions. In addition, the critical magnetic field strength required for actuation in wet environments is generally higher than that in both dry and underwater environments. For  $\varphi = 1.8$ , the critical magnetic

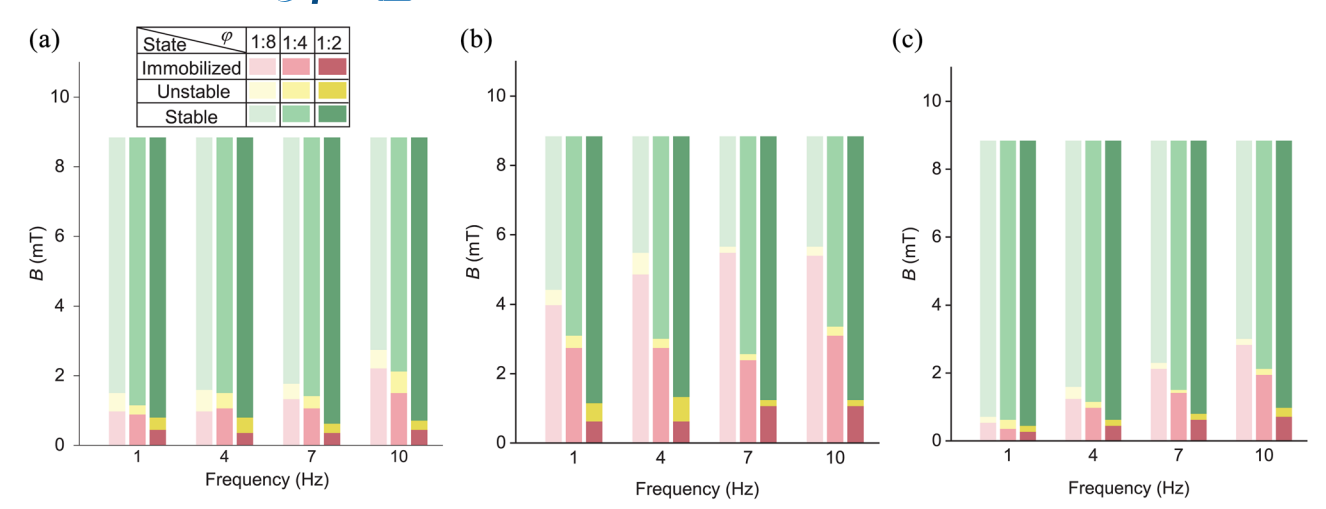


FIGURE 4 Influence of NdFeB microparticle concentration on critical magnetic field strength for the actuation of thermo-magnetic petal morphing robots (TMPMRs) under different environments. (a) Critical magnetic field strength required for TMPMR actuation on a dry surface. (b) Critical magnetic field strength characterization for the TMPMR on a wet surface. (c) Critical magnetic field strength characterization for the TMPMR in an underwater environment. The results highlight how particle concentration affects the required magnetic field for actuation under various conditions.

field strength is  $5.56\pm0.08$  mT in wet conditions under the rotation frequency of 7 Hz, while it is  $1.77\pm0.22$  mT and  $2.21\pm0.09$  mT for dry and underwater environments, respectively. This suggests that the presence of thin liquid film increases the resistance to magnetic actuation, demanding a stronger magnetic field to initiate stable locomotion. Overall, the results highlight that higher NMMPs concentrations lead to a more responsive TMPMR with lower required magnetic field strength, especially in more challenging wet environments, where the reduction in the critical field is most noticeable.

The TMPMR's versatility is further demonstrated in its ability to navigate complex terrains and manipulate cargo. As shown in Figure 5a, the robot successfully traverses slopes, sand, and rocky surfaces, showcasing its adaptability to different terrains (Supporting Information: Movie S1). It is noted that the TMPMR can maintain its high speed with negligible variations for locomotion on various slopes (Supporting Information: Figure S5). The ability to follow precise trajectories, as demonstrated in Figure 5b, further highlights the robot's potential for use in controlled environments where precision is critical. In more complex scenarios, such as maze navigation (Figure 5c), the TMPMR demonstrates its capacity for executing intricate maneuvers under magnetic control (Supporting Information: Movie S2). Additionally, the robot's gripper capability was tested in an in vivo-like drug delivery model, where it successfully transported a medical tablet, which are seven times heavier than our TMPMR, across a simulated stomach without losing its grip (Figure 5d and Supporting Information: Movie S3). The TMPMR's ability to manipulate cargo in challenging environments, including slopes and narrow spaces, is further illustrated in Figure 5e, where it performs a sequence of loading, transportation, and unloading tasks (Supporting Information: Movie S4). The TMPMR's performance in diverse environments underscores its potential for real-world applications. Its ability to handle cargo while navigating complex terrains could be particularly useful in biomedical applications, such as targeted drug delivery in the

gastrointestinal tract, or in industrial settings where precise handling of materials is required. Future work could explore scaling the robot down for minimally invasive medical procedures or scaling it up for larger industrial applications.

# CONCLUSION

The development of TMPMRs introduces a significant advancement in the field of soft robotics, combining the thermal responsiveness of LCEs with the magnetic actuation capabilities provided by NMMPs. Through a synergistic thermal-magnetic actuation mechanism, the TMPMR demonstrates remarkable versatility, achieving both controlled rolling locomotion and reversible shape morphing. Our study reveals that the TMPMR can reliably perform in a variety of environments, including dry, wet, and underwater, with minimal degradation in performance over time. The robot's dual-functional capability of cargo manipulation and high-speed rolling locomotion underscores its potential for realworld applications, particularly in scenarios requiring precision and adaptability, such as biomedical delivery systems or industrial automation tasks. Future research will focus on optimizing the NMMP concentration and refining the shape-morphing dynamics to further enhance the robot's efficiency. Additionally, scaling the robot's design for both microscale biomedical applications and larger industrial systems will open new avenues for deployment in diverse environments.

#### **METHODS**

1,4-Bis-[4-(3-acryloyloxypropypropyloxy)benzoyloxy]-2-methylbenzene (RM257, 98%) was purchased from Leyan Chemicals Inc. Pentaerythritol tetrakis(3-mercaptopropionate) (PETMP, 90%), 2,2-(ethylenedioxy)diethanethiol (97%), (2-hydroxyethoxy)-2-methylpropiophenone (HHMP, 97%), dipropylamine (DPA, 99%), tris(hydroxymethyl)aminomethane (99.8%), DAH (98%), and toluene (99%)

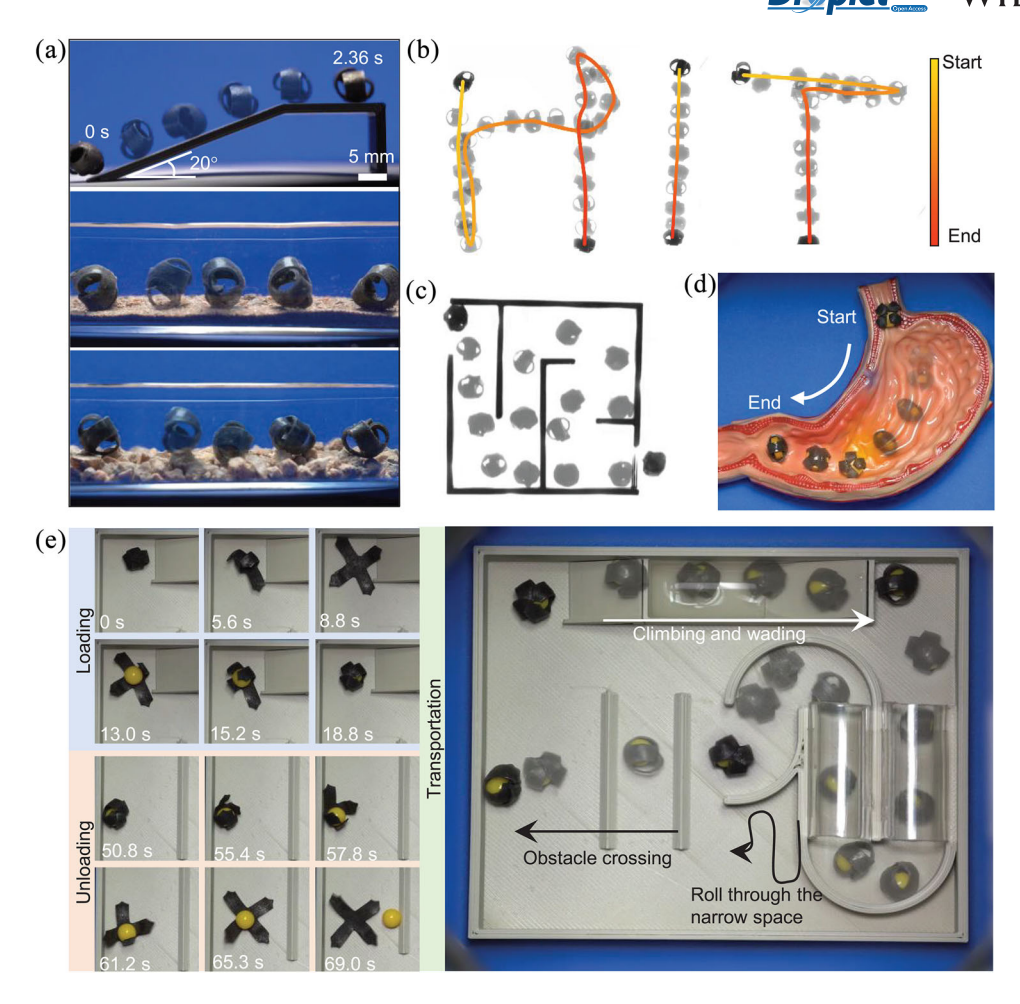


FIGURE 5 Demonstration of the thermo-magnetic petal morphing robot (TMPMR) robust and versatile locomotion and cargo-handling capabilities. (a) Sequential images illustrating the TMPMR's successful traversal of a 20° slope (top), soft sand (middle), and rough rocky surfaces (bottom). (b) High-fidelity maneuvering of the TMPMR, precisely replicating strokes to form the word "HIT." (c) Navigation through a maze, illustrating the TMPMR's precise control and adaptability. (d) In vivo-like drug delivery demonstration, where the TMPMR navigates a complex stomach model, carrying a medical tablet seven times its own weight. (e) Time-lapsed images of the TMPMR performing cargo delivery tasks, including loading, transportation, and unloading, with the TMPMR navigating challenging terrains such as slopes, water, narrow spaces, and obstacles.

were purchased from Aladdin Chemicals Inc. NMMPs (LW-N-11-9) was purchased from Hebei Chaoyue Co., Ltd. All chemicals were used without further purification.

The fabrication of the TMPMR involves a multi-step process that integrates LCEs for thermal actuation, NMMPs for magnetic actuation, and a DAH coating for light-to-thermal energy conversion. The procedure consists of four key stages: composite oligomer synthesis, curing and shaping, formation of the photothermal conversion layer, and magnetization (Supporting Information: Figure S6). In the first step of composite oligomer synthesis, a two-stage TAMAP reaction method was used in this work. So Specifically, 2 g of RM257 was dissolved in 0.8 g of toluene in a transparent glass vial, and the solution was heated to 80°C until RM257 was fully dissolved, yielding a colorless and transparent solution. After cooling the solution to room temperature, 0.109 g of PETMP and 0.458 g of EDDT were added. If any precipitation occurred, the mixture was reheated to 80°C to dissolve the components before cooling it again to room temperature. Next, 0.012 g of the photoinitiator HHMP was added to the solution.

Separately, DPA was dissolved in toluene at a 1:50 weight ratio and vigorously mixed for 1 min. A total of 0.284 g of this DPA solution was then added to the primary vial containing RM257. Following this, NMMPs with different mass ratio  $\varphi$  were introduced into the mixture. The solution was then homogenized using a vortex mixer and degassed in a vacuum chamber at –0.6 MPa for 1 min to remove any bubbles.

Once the solution was prepared, the first stage of polymerization was initiated. The degassed solution was immediately poured into a PTFE mold and left at room temperature in the dark for at least 12 h to allow the initial cross-linking reaction to proceed. Afterward, the cross-linked elastomer, now in a flat cross-like shape, was removed from the mold and placed in a vacuum oven set to –0.6 MPa and 80°C for 24 h to evaporate the remaining toluene. To achieve the desired spherical shape for rolling locomotion, the elastomer was mechanically stretched along two axes and then fixed onto a plastic spherical mold using adhesive tape. This structure was exposed to UV light (365 nm wavelength) for 15 min to initiate the second-stage polymerization

and lock the LC alignment. Once cured, the elastomer was removed from the spherical mold.

After the curing process, a dopamine coating was applied to impart photothermal properties to the TMPMR. The elastomer was submerged in a solution containing 0.1 g of DAH and 0.2 g of tris powder dissolved in 100 mL of deionized water, with the pH adjusted to 8.5. The elastomer was left to soak for 24 h, during which the DAH self-polymerized on the surface, forming a thin photothermal conversion layer.

The final step involved magnetizing the robot to enable controlled rolling under a magnetic field. The prepared TMPMR was dried and magnetized by an impulse magnetic field (3 T) using a magnetizer (MA-2040, Shenzhen JiuJu Industrial Equipments Co., Ltd.). The control voltage of the magnetizer was set at 2 kV, and the TMPMR was subjected to multiple cycles of magnetization to ensure a uniform and strong magnetic field across its structure.

The fabricated TMPMRs were further treated with a commercial coating agent (Glaco Mirror Coat "Zero," Soft 99 Co.) to render the surface superhydrophobic nature. And the contact angle measurement was conducted via a commercial optical contact angle goniometers (OCA 25, DataPhysics Instruments GmbH) in the sessile drop mode.

The hardware architecture of the robotic motion control platform is depicted in Supporting Information: Figure S7. This system comprises a 2D Helmholtz coil assembly, a servo-driven rotation platform, a robotic motion platform, and an integrated vision processing unit. The 2D Helmholtz coil assembly generates a uniform magnetic field, which facilitates the deformation and locomotion of the robot. The servo-driven rotation platform rotates the Helmholtz coils, enabling modulation of the magnetic field direction. Through this rotational actuation, the initially 2D magnetic field generated by the Helmholtz coils is effectively transformed into a 3D magnetic field, which governs the robot's movement on the platform. The robotic motion platform isolates the robot from direct contact with the coils, ensuring that coil rotation affects only the magnetic field without physically interfering with the robot's locomotion. The vision processing unit monitors and regulates the robot's position, velocity, and directional control.

To achieve precise regulation of the coil currents, three DC power supplies independently power the X coil, Z coil, and the rotation platform motor. Power drivers are placed between the power supplies and the corresponding devices, with control signals transmitted to each driver via a data acquisition board (NI-PCIE6738, National Instruments Corp.). The X and Z coils are controlled by servo controllers (G-SOLTWID140/100SRSD, Elmo Motion Control Ltd.), while the rotation platform stepper motor is actuated using a ZD-2HA860 driver (Beijing Times Brilliant Co., Ltd.). Two industrial cameras (MV-CA013-A0GM, Hikvision Digital Technology Co., Ltd.) are positioned along the positive *y*-axis and negative *z*-axis, respectively, to provide real-time monitoring of the robot's position.

The software controlling the robotic motion system was developed using Qt 6.1. Position detection of the robot is achieved through the cameras associated with the X and Z coils, each with a resolution of  $1280\times1024.$  The software captures a frame from the cameras every 30 ms and displays it in the corresponding user interface window. Dur-

ing video recording or when a screenshot is requested, the software utilizes OpenCV's contour detection algorithm to identify all contours within the frame, selecting the contour that most closely matches the expected size of the robot and recording the centroid coordinates. The processed output is subsequently saved either to the video stream or as an image file.

To evaluate the mechanical properties of the LCE/NdFeB composite, tensile tests were performed on samples with various NdFeB-to-LCE mass ratio (1:8, 1:4, 1:2) as well as a control sample without NdFeB. The dog-bone-shaped test samples were fabricated with dimensions shown in Supporting Information: Figure S8, for both after initial crosslinking and after solvent evaporation. Tensile testing was conducted using a ZwickRoell Z010 universal testing machine. The tests were performed at a constant strain rate of 5 mm/min. The magnetic flux density inside the robotic motion platform was measured by using a high-precision digital gaussmeter (HT201, Shanghai Hengtong Magnetoelectricity Co., Ltd.). Besides, the calculation of surface coverage fraction of NdFeB microparticles from the SEM images was performed by using the ImageJ software. NIR light was generated using a 3 W laser module (FU808AD3000-F34, Shenzhen Fuzhe Technology Co., Ltd.), and the thermal images of TMPMR evolution were captured with an infrared camera (FLIR A615) with a close-up 2.9× lens.

#### **ACKNOWLEDGMENTS**

This work was funded by the Shenzhen Science and Technology Program (JCYJ20210324132810026, KQTD20210811090146075, and GXWD20220811164014001), the National Natural Science Foundation of China (52375175 and 52005128), and Guangdong Basic and Applied Basic Research Foundation (2024A1515240015).

### CONFLICT OF INTEREST STATEMENT

The authors declare no conflicts of interest.

# ORCID

Chonglei Hao https://orcid.org/0000-0003-4695-0442

Zuankai Wang https://orcid.org/0000-0002-5810-342X

## **REFERENCES**

- Cianchetti M, Laschi C, Menciassi A, Dario P. Biomedical applications of soft robotics. Nat Rev Mater. 2018;3:143-153.
- Li M, Pal A, Aghakhani A, Pena-Francesch A, Sitti M. Soft actuators for real-world applications. Nat Rev Mater. 2021;7:235-249
- Wang J, Chortos A. Performance metrics for shape-morphing devices. Nat Rev Mater. 2024;9:738-751.
- Wen F, Lee C. Water droplets play a role in Internet of Things applications. Droplet. 2024;3:e133.
- Jiang S, Wu D, Li J, Chu J, Hu Y. Magnetically responsive manipulation of droplets and bubbles. *Droplet*. 2024;3:e117.
- Rich SI, Wood RJ, Majidi C. Untethered soft robotics. Nat Electron. 2018;1:102-112.
- Wang Y, Liu J, Yang S. Multi-functional liquid crystal elastomer composites. Appl Phys Rev. 2022;9:011301.
- He Q, Wang Z, Wang Y, Song Z, Cai S. Recyclable and self-repairable fluid-driven liquid crystal elastomer actuator. ACS Appl Mater Interfaces. 2020;12:35464-35474.

- Feng W, He Q, Zhang L. Embedded physical intelligence in liquid crystalline polymer actuators and robots. Adv Mater. 2025;37:e2312313.
- White TJ, Broer DJ. Programmable and adaptive mechanics with liquid crystal polymer networks and elastomers. *Nat Mater.* 2015;14:1087-1098.
- Davidson ZS, Shahsavan H, Aghakhani A, et al. Monolithic shapeprogrammable dielectric liquid crystal elastomer actuators. Sci Adv. 2019;5:eaay0855.
- 12. Zhao Y, Chi Y, Hong Y, Li Y, Yang S, Yin J. Twisting for soft intelligent autonomous robot in unstructured environments. *Proc Natl Acad Sci U S A*. 2022;119:e2200265119.
- 13. Guin T, Settle MJ, Kowalski BA, et al. Layered liquid crystal elastomer actuators. *Nat Commun*. 2018;9:2531.
- Kotikian A, Morales JM, Lu A, et al. Innervated, self-sensing liquid crystal elastomer actuators with closed loop control. Adv Mater. 2021;33:2101814.
- Maurin V, Chang Y, Ze Q, Leanza S, Wang J, Zhao RR. Liquid crystal elastomer-liquid metal composite: ultrafast, untethered, and programmable actuation by induction heating. Adv Mater. 2024;36:2302765.
- He Q, Wang Z, Wang Y, Minori A, Tolley MT, Cai S. Electrically controlled liquid crystal elastomer-based soft tubular actuator with multimodal actuation. Sci Adv. 2019;5:eaax5746.
- Kim H, Lee JA, Ambulo CP, et al. Intelligently actuating liquid crystal elastomer-carbon nanotube composites. Adv Funct Mater. 2019:29:1905063.
- Xia Y, Cedillo-Servin G, Kamien RD, Yang S. Guided folding of nematic liquid crystal elastomer sheets into 3D via patterned 1D microchannels. Adv Mater. 2016;28:9637-9643.
- Wang Z, Wang Z, Zheng Y, He Q, Wang Y, Cai S. Three-dimensional printing of functionally graded liquid crystal elastomer. Sci Adv. 2020;6:eabc0034.
- Hu W, Lum GZ, Mastrangeli M, Sitti M. Small-scale soft-bodied robot with multimodal locomotion. *Nature*. 2018;554:81-85.
- 21. Mao G, Schiller D, Danninger D, et al. Ultrafast small-scale soft electromagnetic robots. *Nat Commun*. 2022;13:4456.
- Xu C, Yang Z, Tan SWK, Li J, Lum GZ. Magnetic miniature actuators with six-degrees-of-freedom multimodal soft-bodied locomotion. Adv Intell Syst. 2022;4:2100259.
- 23. Xia N, Jin B, Jin D, et al. Decoupling and reprogramming the wiggling motion of midge larvae using a soft robotic platform. *Adv Mater*. 2022;34:2109126.
- 24. Li G, Zhang T, Shen Y. Transparent magnetic soft millirobot actuated by micro-node array. *Adv Mater Technol*. 2021;6:2100131.
- Lu H, Zhang M, Yang Y, et al. A bioinspired multilegged soft millirobot that functions in both dry and wet conditions. *Nat Commun*. 2018;9:3944.
- Zhang J, Guo Y, Hu W, Soon RH, Davidson ZS, Sitti M. Liquid crystal elastomer-based magnetic composite films for reconfigurable shapemorphing soft miniature machines. Adv Mater. 2021;33:2006191.
- Zhang J, Ren Z, Hu W, et al. Voxelated three-dimensional miniature magnetic soft machines via multimaterial heterogeneous assembly. Sci Rob. 2021;6:eabf0112.
- 28. Siebenmorgen C, Wang C, Navarro LB, et al. Minimally designed thermo-magnetic dual responsive soft robots for complex applications. *J Mater Chem B.* 2024;12:5339-5349.
- Li Y, Yu H, Yu K, Guo X, Wang X. Reconfigurable three-dimensional mesotructures of spatially programmed liquid crystal elastomers and their ferromagnetic composites. *Adv Funct Mater.* 2021;31:2100338.
- Ford MJ, Ambulo CP, Kent TA, et al. A multifunctional shape-morphing elastomer with liquid metal inclusions. Proc Natl Acad Sci U S A. 2019;116:21438-21444.
- 31. Kotikian A, McMahan C, Davidson EC, et al. Untethered soft robotic matter with passive control of shape morphing and propulsion. *Sci Rob.* 2019;4:eaax7044.

- Lu X, Guo S, Tong X, Xia H, Zhao Y. Tunable photocontrolled motions using stored strain energy in malleable azobenzene liquid crystalline polymer actuators. Adv Mater. 2017;29:1606467.
- Boothby JM, Gagnon JC, McDowell E, Van Volkenburg T, Currano L, Xia Z. An untethered soft robot based on liquid crystal elastomers. Soft Rob. 2022;9:154-162.
- 34. Yang X, Chen Y, Zhang X, et al. Bioinspired light-fueled water-walking soft robots based on liquid crystal network actuators with polymerizable miniaturized gold nanorods. *Nano Today*. 2022;43:101419.
- Zeng H, Wani OM, Wasylczyk P, Priimagi A. Light-driven, caterpillarinspired miniature inching robot. *Macromol Rapid Commun*. 2018;39:1700224.
- 36. Zhou X, Chen G, Jin B, et al. Multimodal autonomous locomotion of liquid crystal elastomer soft robot. *Adv Sci.* 2024;11:2402358.
- Zhao T, Wang J, Fan Y, Dou W. Helical liquid crystal elastomer miniature robot with photocontrolled locomotion. Adv Mater Technol. 2022;7:2200222.
- Qian N, Bisoyi HK, Wang M, et al. A visible and near-infrared lightfueled omnidirectional twist-bend crawling robot. Adv Funct Mater. 2023;33:2214205.
- Wu S, Hong Y, Zhao Y, Yin J, Zhu Y. Caterpillar-inspired soft crawling robot with distributed programmable thermal actuation. Sci Adv. 2023;9:eadf8014.
- Gu H, Boehler Q, Cui H, et al. Magnetic cilia carpets with programmable metachronal waves. Nat Commun. 2020;11:2637.
- 41. Niu H, Feng R, Xie Y, et al. Magworm: a biomimetic magnet embedded worm-like soft robot. *Soft Rob.* 2021;8:507-518.
- 42. Ju Y, Hu R, Xie Y, et al. Reconfigurable magnetic soft robots with multimodal locomotion. *Nano Energy*. 2021;87:106169.
- Joyee EB, Pan Y. A fully three-dimensional printed inchworm-inspired soft robot with magnetic actuation. Soft Rob. 2019;6:333-345.
- Wang C, Puranam VR, Misra S, Venkiteswaran VK. A snake-inspired multi-segmented magnetic soft robot towards medical applications. IEEE Rob Autom Lett. 2022;7:5795-5802.
- Karipoth P, Christou A, Pullanchiyodan A, Dahiya R. Bioinspired inchworm- and earthworm-like soft robots with intrinsic strain sensing. Adv Intell Syst. 2022;4:2100092.
- Kim Y, Yuk H, Zhao R, Chester SA, Zhao X. Printing ferromagnetic domains for untethered fast-transforming soft materials. *Nature*. 2018:558:274-279.
- 47. Yim S, Sitti M. Design and rolling locomotion of a magnetically actuated soft capsule endoscope. *IEEE Trans Rob.* 2012;28:183-194.
- Huang H-W, Sakar MS, Petruska AJ, Pané S, Nelson BJ. Soft micromachines with programmable motility and morphology. *Nat Commun*. 2016;7:12263.
- Ren Z, Hu W, Dong X, Sitti M. Multi-functional soft-bodied jellyfish-like swimming. Nat Commun. 2019;10:2703.
- Saed MO, Torbati AH, Nair DP, Yakacki CM. Synthesis of programmable main-chain liquid-crystalline elastomers using a two-stage thiol-acrylate reaction. J Vis Exp. 2016;19:e53546.

# SUPPORTING INFORMATION

Additional supporting information can be found online in the Supporting Information section at the end of this article.

**How to cite this article:** Wang Y, Yang S, Hao C, et al. Thermo-magnetic soft robot for adaptive locomotion and delivery. *Droplet*. 2025;4:e70016.

https://doi.org/10.1002/dro2.70016